Electronic modulation and vacancy engineering of Ni$_9$S$_8$ to synergistically boost efficient water splitting: Active vacancy-metal pairs

Qin Gao [1], Wei Luo [1], Xueying Ma, Zemian Ma, Sijun Li, Fenglin Gou, Wei Shen, Yimin Jiang, Rongxing He [*], Ming Li [*]

Key Laboratory of Luminescence Analysis and Molecular Sensing (Southwest University), Ministry of Education, College of Chemistry and Chemical Engineering, Southwest University, Chongqing 400715, PR China

ABSTRACT

Developing easy-to-make and excellent bifunctional electrocatalysts for water splitting over a wide pH range is a challenging yet appealing topic. Herein, based on integration of vacancy engineering and electronic modulation, a high-performance v$_s$-Ru-Ni$_9$S$_8$ electrocatalyst for water splitting was constructed via a cost-effective one-step hydrothermal method. Under the synergistic regulation of Ru-doping and sulfur vacancies, the v$_s$-Ru-Ni$_9$S$_8$ exhibited the outstanding electrocatalytic performance and long-time durability, along with ultra-low OER overpotentials of 218 and 268 mV at 100 and 300 mA cm^{-2} in alkaline electrolyte and low HER overpotentials of 56, 131, 94 mV at 10 mA cm^{-2} in acidic, neutral, alkaline electrolyte. Impressively, 1.47 and 1.68 V of voltages were needed to achieve 10 and 300 mA cm^{-2} for the v$_s$-Ru-Ni$_9$S$_8$ (+, -) cell. Our DFT results revealed that the doping Ru atom played a crucial role in regulating electron density in OER, rather than served as a catalytic active site. More importantly, we corroborated the active Ni-vacancy pair composed of Ni atom and sulfur vacancy, as an active site, and its catalytic synergy in OER. Especially, a vacancy-metal synergetic mechanism for OER was suggested to correctly describe the OER process and the role of vacancy in catalytic process. Our work provides a simple and effective strategy for fabricating high-performance catalysts and an in-depth understanding of OER.

1. Introduction

In view of the continuous depletion of fossil fuels and their harmful effects on the environment, it is increasingly urgent to deeply study innovative technologies for sustainable clean energy conversion and storage [1–3]. The water electrocatalytic splitting is an environment-friendly, efficient, and promising technology to generate hydrogen energy with no carbon emission and high energy density [4–8]. There are two half-reactions for water electrolysis corresponding to hydrogen evolution reaction (HER) in the cathode and oxygen evolution reaction (OER) in the anode. Unfortunately, the sluggish kinetics of the OER requires a high overpotential to achieve considerable current density, leading to low energy conversion efficiency [9–12]. Therefore, constructing superior-performance electrocatalysts for the OER is very urgent to reduce energy consumption and improve hydrogen production efficiency.

In the past decades, great efforts have been made to fabricate highly active transition metal catalysts, including phosphides [13,14], nitrides [15,16], carbides [17,18], sulfides [19–21] and (oxy)hydroxides [22, 23], in order to significantly promote water electrolysis. Transition metal sulfides, especially nickel-based sulfides, have attracted extensive attention due to their special D-electron structures, low prices, and high electrical conductivity and are considered as promising electrocatalysts for water electrolysis [24,25]. A variety of synthetic strategies were employed to construct excellent nickel-based sulfide catalysts to reduce overpotentials of catalysis and promote the catalytic process for both the HER and the OER. For example, introducing heteroatoms into nickel-based sulfide catalysts is a prospective strategy to optimize the intrinsic catalytic activity by modulating their electron densities. Wang et al. synthesized the porous Ni$_9$S$_8$ material coupled with N and S co-doped carbon nanoparticles via a wet-chemical method and thermal decomposing, which exhibited a good catalytic performance with an overpotential of 280 mV at a current density of 10 mA cm^{-2} for the OER [26]. Chen et al. prepared nano flower balls Ni$_3$S$_2$ catalyst in the

---

* Corresponding authors.
E-mail addresses: herx@swu.edu.cn (R. He), liming@swu.edu.cn (M. Li).
[1] These authors contributed equally to this work.

presence of the Mo element through a two-step hydrothermal method, needing overpotentials of 115 and 222 mV to yield a current density of 10 mA cm^{-2} toward the HER and OER [27]. The vacancy engineering strategy is also widely employed to enhance the catalytic activity by exposing more active sites on the surfaces of catalysts. Jia et al. designed a porous Ni_3S_2 nanosheet with rich sulfur vacancies, v_s-Ni_3S_2/NF, by a plasma-assisted process, exhibiting a superior alkaline HER catalytic activity, which only required the overpotential of 88 mV to afford a current density of 10 mA cm^{-2} [28]. Thus it is clear that both the doping and the vacancy engineering are efficient strategies to elevate the catalytic activity.

As you can imagine, utilizing heteroatom doping and vacancy engineering to synergistically regulate the surface activity of catalysts should be an effective strategy to construct excellent catalysts for both HER and OER. During the catalytic process, doping atoms either plays a role in regulating the electron density of the catalyst, or serves as catalytic active sites, or both, whereas vacancies not only regulate the electron density, but also lead to the exposure of more active sites, which is conducive to improving the catalytic performance. Using these two strategies to construct catalytic materials and the in-depth study of their synergistic effects in facilitating the catalytic activity must be of great significance to the fabrication of highly efficiency catalysts. However, many researches on nickel sulfide-based materials only focused on one of the above aforementioned strategies, leading to more experimental spaces in improving catalytic activity and to the fuzziness of the catalytic mechanism of the multi-strategy mutual effect. Furthermore, the synthesis steps for these catalysts with an enhanced catalytic activity regulated by multiple strategies are usually cumbersome and environment-unfriendly, and toxic sulfur gas may be released in the vulcanization process. Therefore, it is urgent to construct highly active nickel-based sulfide electrocatalysts by an economical and effective ordinary approach, which integrates heteroatom doping with vacancy engineering, but it is still a huge challenge.

Herein, for the first time, we transformed successfully the Ni_9S_8 material with poor activity into a significantly efficient electrocatalyst for water splitting by integration of trace ruthenium doping and sulfur vacancy engineering via a cost-effective one-step hydrothermal method. As expected, the as-prepared Ru-doped nickel-based sulfide electrocatalyst with rich sulfur vacancies, v_s-Ru-Ni_9S_8, displayed an prominent HER performance over a wide pH range and an outstanding alkaline OER performance at a high current density. Meanwhile, our density functional theory computations displayed the important role of the doping Ru atom in regulating electron density in the OER, rather than as a catalytic active site. More importantly, we corroborated the active nickel-vacancy pair composed of Ni atom and sulfur vacancy as an active site and its catalytic synergy in the OER.

2. Experimental sections

2.1. Synthesis of Ru-Ni_9S_8 and v_s-Ru-Ni_9S_8 on NF

Trace-Ru-doped nickel sulfide electrocatalyst, Ru-Ni_9S_8, was generated by one-step hydrothermal procedure. Before the reaction, the Ni foam (1 cm × 3 cm) was ultrasonicated in acetone, ethanol, 3 M HCl solution, and deionized water successively to slough off surface impurities. $Na_2S_2O_3$.5 H_2O (75 mg) and $RuCl_3$·xH_2O (7 mg) were dissolved in 20 mL deionized water and stirred continuously to obtain a homogeneous solution. A piece of pretreated Ni foam was placed in this homogeneous solution and transferred to a 50 mL Teflon-lined stainless steel autoclave, which was heated at 140 °C for 6 h. When the reaction products are cooled to room temperature, the black nickel foam was washed for several times with distilled water and ethanol. The black nickel foam was dried in vacuum at 60 °C about 12 h and named as the Ru-Ni_9S_8. The v_s-Ru-Ni_9S_8 with rich sulfur vacancies was synthesized in a similar way, except that the reaction temperature is 100 °C.

2.2. Synthesis of Ru-Ni_9S_8 and v_s-Ru-Ni_9S_8 on CP

Firstly, the powder catalysts of Ru-Ni_9S_8 and v_s-Ru-Ni_9S_8 were, respectively, scraped off the NF (1 ×1 cm^2) loaded with the catalysts. The scraped powder catalysts were added to the solution of 490 μL alcohol and 10 μL 5% Nafion, which was sonicated for 30 min to form uniformly dispersed ink solution. Subsequently, 500 μL of the ink was covered on the carbon paper (CP) (1 × 1 cm^2). Finally, the carbon paper loaded with catalysts was air-dried at room temperature. The catalyst-loaded CP (1 × 1 cm^2) electrodes were served as the working electrodes in acidic condition.

2.3. Characterization

XRD data for as-prepared samples were measured on a D2 PHASER X-ray diffractometer with Cu Kα radiation. SEM tests were conducted on a XL30 ESEM FEG scanning electron microscope. TEM and HRTEM images were acquired by a use of a JEOL JEM 2100 F. XPS was measured on a Thermo Scientific K-Alpha+. EPR measurements were taken on a Bruker EMXnano spectrometer at room temperature. The analysis of element content was achieved by ICPMS, Agilent 7800.

2.4. Electrochemical measurements

Related electrochemical experiments were conducted on a CHI 660E electrochemical workstation equipped with a three-electrode cell. The catalyst-loaded NF (1 × 1 cm), graphite rods and mercury mercuric oxide (Hg/HgO) electrodes were served as the working, counter and reference electrodes in alkaline solution and phosphate-buffered saline (PBS) condition, respectively. Since NF is easily corroded by 0.5 m H_2SO_4, however, the chronoamperometry response was carried out by the catalyst-loaded carbon paper (CP) in acidic condition. The linear sweep voltammetry (LSV) curves with iR correction were conducted with a sweep rate of 2 mV s^{-1}. Overall water splitting activity was evaluated by a use of the catalyst-supported NF as bifunctional catalysts in an alkaline two-electrode electrolyzer. As a control, RuO_2 (loaded on NF with 2.5 mg cm^{-2}) and Pt/C (loaded on NF with 2.5 mg cm^{-2}) were tested as the anode and the cathode. The electrochemical impedance spectroscopy (EIS) was conducted at the applied potential (1.43 V vs. RHE) in a frequency range from 100 kHz to 1mHz. The double layer capacitance (C_{dl}) derived from the cyclic voltammetry (CV) cures at different scan rates (60–100 mV s^{-1}) was considered as assessing electrochemically active surface area (ECSA). The C_{dl} was estimated by plotting the current density difference at 0.05 V vs. RHE against scan rates. The TOF values were obtained from the equation: TOF $= \frac{I}{mFn}$ [29], where I is the current, F means Faraday's constant and m implies the number of electrons required for water to generate a H_2 or O_2 molecule. n is the quantity of active sites, which can be measured by a formerly reported method, $n = \frac{Q}{2F}$ [30,31]. All voltages were converted to the potential relative to a standard hydrogen electrode by the following formula: $E_{versus RHE} = E_{versus Hg/HgO} + 0.098 + 0.05916 \times pH$ or $E_{versus RHE} = E_{versus Ag/AgCl} + 0.197 + 0.05916 \times pH$.

2.5. DFT calculations

The Vienna ab initio simulation package, which involve Perdew-Burke-Ernzerhof and generalized gradient approximation [32], was employed to implement the density functional theory (DFT) computations of all the reaction intermediates. The cutoff energy was set to 400 eV for the plane wave basis. The convergence thresholds were set to 0.02 eV Å^{-1} in the force and 10^{-6} eV in the energy, respectively. A (2 × 2 × 1) Monkhorst-Pack Gamma-centered k-points mesh was constructed for the DFT computations. The vacuum separation was set to larger than 15 Å.

3. Results and discussion

The synthesis of the layered rock-like v_s-Ru-Ni$_9$S$_8$ on NF is to chemically corrode nickel foam (NF) with Na$_2$S$_2$O$_3$.5H$_2$O at 100 °C in the presence of Ru, as illustrated in Scheme 1. This low-temperature hydrothermal vulcanization results in abundant sulfur vacancies in the Ru-Ni$_9$S$_8$ sample.

3.1. Characterization of as-prepared samples

The micromorphologies of as-synthesized samples were observed by scanning electron microscope (SEM). As shown in Fig. 1a and b, the layered rock-like v_s-Ru-Ni$_9$S$_8$ sample grows uniformly on the nickel foam (NF). The incorporated Ru and sulfur defects promote the transformation of micron particles clusters of the Ni$_9$S$_8$ into regular micron sheets of the v_s-Ru-Ni$_9$S$_8$ observed in Fig. S2, which leads to the exposure of more active sites and facilitates the stability of the catalyst. The transmission electron microscopy (TEM) of the layered rock-like v_s-Ru-Ni$_9$S$_8$ reveals its thin 2D nanosheet structure (Fig. 1c). The HRTEM pattern in Fig. 1d and f shows a interplanar spacing of 0.285 nm consistent well with the (222) crystal plane of the Ni$_9$S$_8$. The selected area electron diffraction (SAED) image of the v_s-Ru-Ni$_9$S$_8$ displays a series of diffraction rings indexed to the (006), (153), and (222) lattice planes of the Ni$_9$S$_8$ (Fig. 1f). The energy dispersive spectroscopy (EDS) spectrum, XPS survey spectra and elemental mapping images (Figs. S1 and 1e) illustrate the presence of the Ni, Ru, and S elements and the uniform distribution of these elements on the whole nanosheet of the v_s-Ru-Ni$_9$S$_8$. The contents of Ni, Ru, and S are respectively 44.2 wt%, 4.5 wt%, and 6.5 wt%, based on (ICP-OES) analysis.

The crystalline structures of the as-made samples were observed by using the X-ray diffraction (XRD). As displayed in Fig. 2a, except for the two diffraction peaks (44.51°, 51.85°) assigned to NF (JCPDS 04–0850), the main peaks centered at 27.2°, 31.4°, 38.6°, 50.6° and 56.6° for the Ni$_9$S$_8$, Ru-Ni$_9$S$_8$, and v_s-Ru-Ni$_9$S$_8$ are detected, coinciding well with (202), (222), (241), (153) and (531) facets of the Ni$_9$S$_8$ (JCPDS:22–1193), respectively. It is noteworthy that the diffraction peaks of the v_s-Ru-Ni$_9$S$_8$ is slightly shifted to a higher diffraction angle, compared with that of the pristine Ni$_9$S$_8$, which may be attributed to the formation of vacancies (Fig. 2b) [33,34]. Meanwhile, no diffraction peaks of Ru element or Ru compounds were found, due to the minimal amount of Ru element, coinciding with ICP-OES result [35,36]. In addition, the weaker peak intensity and wider XRD peak width of the v_s-Ru-Ni$_9$S$_8$ relative to those of the Ru-Ni$_9$S$_8$ may be due to the formation of more sulfur defects.

The EPR and XPS tests for the as-prepared samples were carried out to confirm the presence of sulfur vacancies in the v_s-Ru-Ni$_9$S$_8$ catalyst and determine the valence states and near-surface compositions of the as-prepared samples. As shown in Fig. 2c, the v_s-Ru-Ni$_9$S$_8$ and v_s-Ni$_9$S$_8$ exhibit a strongly symmetrical EPR signal with g= 2.003, but the Ru-Ni$_9$S$_8$ does not, implying that rich sulfur vacancies are generated in the v_s-Ru-Ni$_9$S$_8$ and v_s-Ni$_9$S$_8$ catalysts [37,38]. The formation of numerous sulfur vacancies in the v_s-Ru-Ni$_9$S$_8$ can promote the rapid ion transfer and more active sites, resulting in the outstanding surface reaction kinetics in sustainable energy conversion and storage system [39]. Sulfur vacancies can further be verified by the XPS spectrum. As illustrated in Fig. 2d, compared with those of the Ru-Ni$_9$S$_8$, the Ni 2p$_{1/2}$ (873.7 eV) and Ni 2p$_{3/2}$ (855.7 eV) XPS peaks of the v_s-Ru-Ni$_9$S$_8$ attributable to its Ni–S bond are shifted negatively by about 0.12 and 0.09 eV, respectively, implying an increased electron density of Ni and a lower Ni chemical valence in the v_s-Ru-Ni$_9$S$_8$. The lower Ni chemical valence in the v_s-Ru-Ni$_9$S$_8$ is due to the sulfur vacancies [28,37]. It should be pointed out here that sulfur vacancies of the as-prepared samples can be effectively adjusted by controlling the reaction temperature (Fig. S11). In the high-resolution Ni 2p XPS spectra of the v_s-Ru-Ni$_9$S$_8$, the Ni 2p$_{3/2}$ peak at 855.7 eV and the Ni 2p$_{1/2}$ peak at 873.3 eV are indexed to the Ni^{2+}, respectively, whereas the Ni 2p$_{3/2}$ and Ni 2p$_{1/2}$ peaks at 857.1 and 874.78 eV are assigned to the Ni^{3+} [25,40]. The strong satellite peaks at 861.8 eV and 879.6 eV indicate that the Ni^{2+} state is dominant in the Ni 2 P spectrum [41]. The coexistence of the Ni^{2+} and Ni^{3+} in the as-prepared catalysts may result in the redox reaction on the surface of catalyst and promote the electron transfer, conducive to the efficient electrocatalytic reaction [42]. Furthermore, compared with those of the pristine Ni$_9$S$_8$, the Ni^{2+} 2p$_{3/2}$ and Ni^{2+} 2p$_{1/2}$ peaks assigned to the Ni–S bond of the Ru-Ni$_9$S$_8$ significantly shift positively by 0.98 and 0.76 eV, corroborating that the trace Ru-doping facilitates considerably the redistribution of electron densities for the Ni sites [43,44]. The electronic modulation of the Ru doping on the catalyst can significantly improve its catalytic activity. Fig. 2e exhibits the core-level S2p spectrum of the v_s-Ru-Ni$_9$S$_8$, in which the peaks at 162.4 eV, 163.5 eV, 166.8 eV, and 168.1 eV are identified as S^{2-} 2p$_{3/2}$, S^{2-} 2p$_{1/2}$, S$_n^{2-}$ and SO$_x$, respectively [26,45,46]. The S^{2-} 2p$_{1/2}$ and S^{2-} 2p$_{3/2}$ peaks of the Ru-Ni$_9$S$_8$ display the negative shifts of 0.08 eV and 0.15 eV, compared with those of the pristine Ni$_9$S$_8$, indicating that the Ru-doping also has an effect on the electronic structure of S [31]. Likewise, by comparison of the S^{2-} 2p$_{3/2}$ and S^{2-} 2p$_{1/2}$ peaks of the Ru-Ni$_9$S$_8$ and v_s-Ru-Ni$_9$S$_8$, the significant positive shifts of 0.58 eV and 0.56 eV in the v_s-Ru-Ni$_9$S$_8$ are observed, showing that sulfur vacancies influence remarkably the electronic structure of S species and lead to more partial positive charges of S$^{\delta+}$ [39,47]. In addition, in the Ru 3p XPS spectrum (Fig. S3), the binding energies at 462.0 eV and 484.1 eV are assigned to the Ru^{3+} 3p$_{3/2}$ and Ru^{3+} 3p$_{1/2}$ in the v_s-Ru-Ni$_9$S$_8$, illustrating that Ru is in +3 oxidation state [43,48]. It is clear from the XPS and EPR that Ru element and sulfur vacancies are successfully introduced into the Ni$_9$S$_8$ and have a strong impact on its electronic structure.
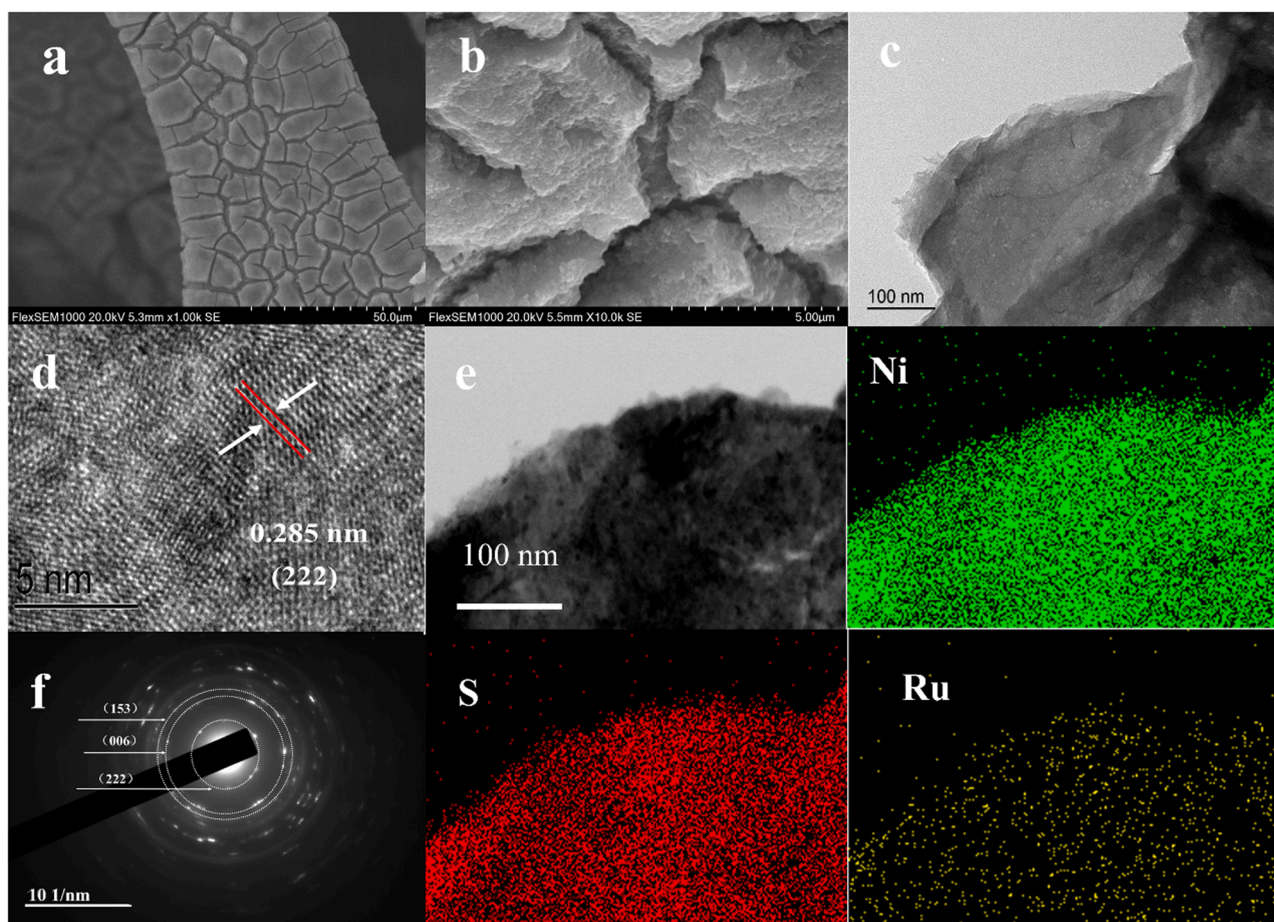
3.2. Electrochemical performance

3.2.1. OER performance

The alkaline OER performances of the as-prepared electrocatalysts were assessed in the routine three-electrode system in 1.0 M KOH
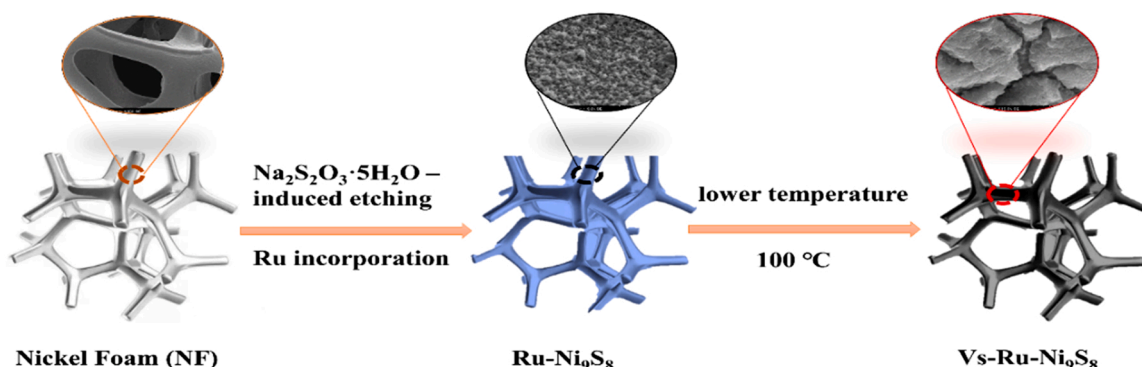
Scheme 1. Schematic illustration for growth of the layered rock-like v_s-Ru-Ni$_9$S$_8$ on NF.

Fig. 1. (a,b) SEM, (c) TEM, and (d) HRTEM patterns of v_s-Ru-Ni$_9$S$_8$. (e) SEM pattern of v_s-Ru-Ni$_9$S$_8$ and the element distribution of Ni, S, Ru, and (f) SAED pattern of v_s-Ru-Ni$_9$S$_8$.

media. As presented in Fig. 3a and b, in contrast with an overpotential of about 490 mV for the pristine Ni$_9$S$_8$, the v_s-Ni$_9$S$_8$, Ru-Ni$_9$S$_8$ and v_s-Ru-Ni$_9$S$_8$, exhibit the substantially decreased OER overpotentials of 400, 296 and 218 mV to reach current density of 100 mA m^{-2}. This result reveals that the trace Ru-doping and sulfur vacancies lead to the significant advance of the OER activity via its electronic modulation of active sites. It is noteworthy that the v_s-Ru-Ni$_9$S$_8$ catalyst based on integration of vacancy engineering and electronic modulation shows much better OER catalytic performance than the Ru-Ni$_9$S$_8$ and v_s-Ni$_9$S$_8$. At high current densities of 100, 200, and 300 mA m^{-2}, the v_s-Ru-Ni$_9$S$_8$ merely requires the OER overpotentials of 218, 249, and 268 mV, far better than the Ru-Ni$_9$S$_8$ without sulfur vacancies (296, 327, and 383 mV), and significantly superior to RuO$_2$ (326, 393, and 450 mV), v_s-Ni$_9$S$_8$ (400 mV, no activity) and Ni$_9$S$_8$ (490 mV, no activity) (Fig. 3b). It is clear that sulfur vacancies have a great effect on the electrocatalytic activity. Obviously, by doping the trace Ru element and effectively adjusting sulfur vacancies in the pristine Ni$_9$S$_8$, a high-performance nickel-based electrocatalyst for water splitting is fabricated, and its OER performance is much better than the overwhelming majority of reported nickel-based catalysts (Table S1 in Supporting Information). The Tafel slope is employed to access the catalytic reaction kinetics, and generally, a small Tafel slope is in line with the fast reaction kinetics. The Tafel slope of the v_s-Ru-Ni$_9$S$_8$ is 77.6 mV dec^{-1} and much lower than 226.1 mV dec^{-1} of the Ni$_9$S$_8$, 212.1 mV dec^{-1} of the v_s-Ni$_9$S$_8$, 200.1 mV dec^{-1} of the RuO$_2$, 130.1 mV dec^{-1} of the Ru-Ni$_9$S$_8$ (Fig. 3c), showing a faster catalytic reaction kinetics for the v_s-Ru-Ni$_9$S$_8$ catalyst. The long-time durability of catalysts is also a crucial indicator to assess the electrocatalytic performance. As illustrated in Fig. 3d, compared with that of the RuO$_2$, the stable current density of about 100 mA cm^{-2}

for the v_s-Ru-Ni$_9$S$_8$ has the negligible decay during 30 h continuous testing at a fixed voltage, corroborating the long-time durability of the v_s-Ru-Ni$_9$S$_8$. Furthermore, in Fig. S4b, the LSV curves and morphology of the v_s-Ru-Ni$_9$S$_8$ after 1000 CV cycles keep intact, further validating the prominent durability of the v_s-Ru-Ni$_9$S$_8$ for OER.

The XPS of the as-prepared catalysts for the post-OER were measured to provide an insight into their outstanding OER catalytic activity. As described in Fig. 4a, the deconvolution peaks of the O 1 s spectrum for the v_s-Ru-Ni$_9$S$_8$ verify the formation of the Ni-O bonds after the OER. The situ electrochemical oxidation of the Ni$_9$S$_8$ during the OER results in the formation of the NiO phase on the surface of the catalyst [49–51], and the formed NiO species serve as the electrochemically active sites for the OER [31,49,52]. The S 2p XPS spectra of the v_s-Ru-Ni$_9$S$_8$ after 15 min and 60 min durability tests toward the OER in 1.0 M KOH are shown in Fig. 4b. The current density tends to be stable after the OER stability test for 15 min and the Ni sulfide signal in the S 2p region is significantly weakened, accompanied by the appearance of the S-O signal, whereas the Ni sulfide signal vanishes totally after the 60 min stability tests. These experimental results reveal that the surface electrochemical oxidation of original Ni sulfides into Ni oxides occurs and leads to the formation of the interfaces between Ni-oxides and Ni-sulfides, which promotes the adsorption of OH$^-$ and thus the OER activity [53–55]. Further, as shown in Fig. 4b, after the stability test for 15 min, the Ni sulfide signal for the v_s-Ru-Ni$_9$S$_8$ with rich sulfur vacancies is much weaker than that for the Ru-Ni$_9$S$_8$ without sulfur vacancies, implying that the v_s-Ru-Ni$_9$S$_8$ undergoes a faster surface electrochemical oxidation and thus exhibits the better OER catalytic performance. In addition, in the high-resolution Ni 2 P XPS spectrum (Fig. 2d), the signal for Ni^{3+} of the v_s-Ru-Ni$_9$S$_8$ is much stronger than

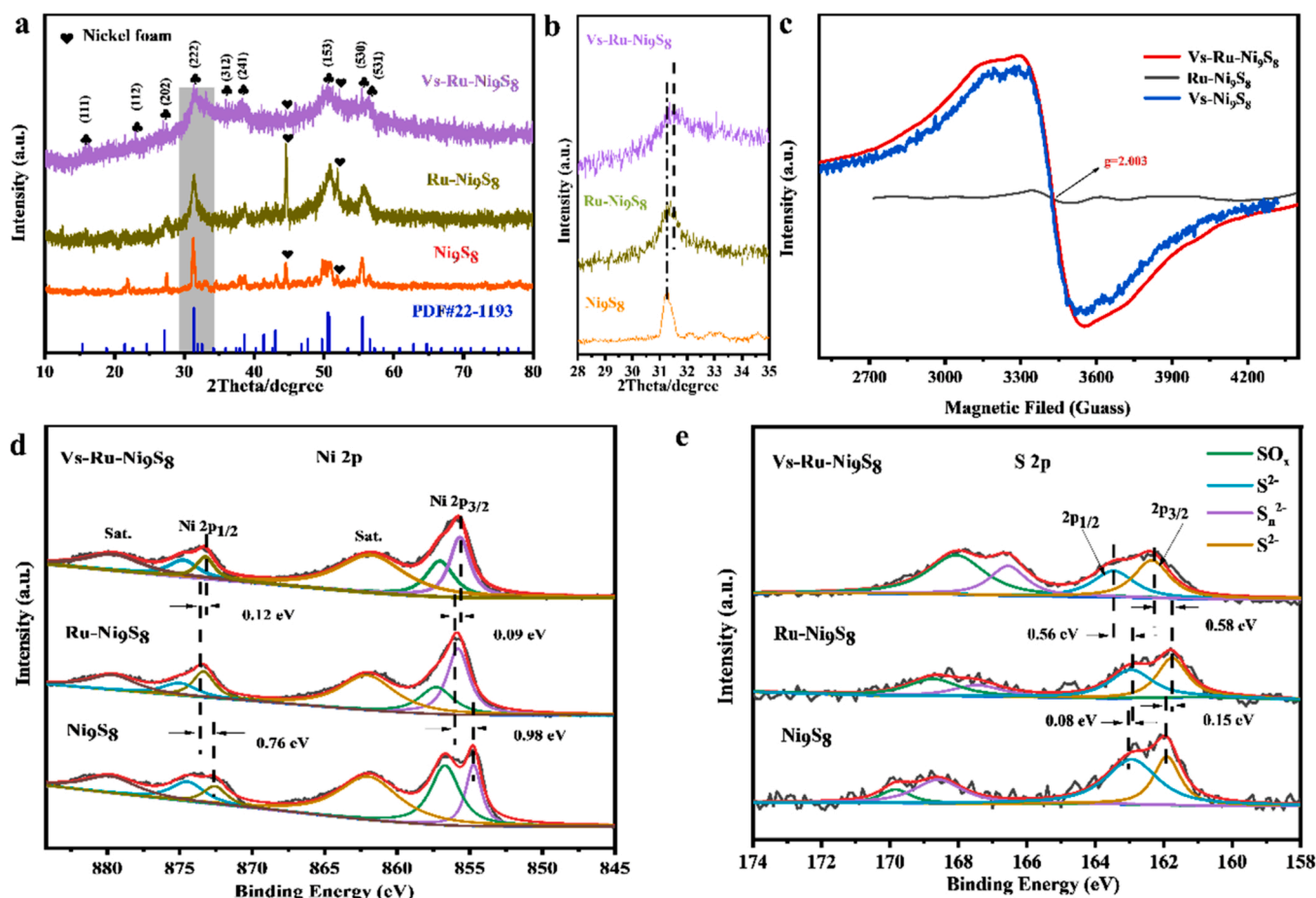**Fig. 2.** (a) XRD patterns and (b) enlarged XRD patterns. (c) EPR spectra. (d) Ni 2p and (e) S 2p high-resolution XPS spectra.

that of the Ru-Ni$_9$S$_8$, indicating that the v$_s$-Ru-Ni$_9$S$_8$ may involve an easier surface Ni-oxidation [56].

The double-layer capacitances (C$_{dl}$) are positively related to the effective electrochemical active surface areas (ECSAs) of the catalyst, and the larger the ECSAs, the more active sites exposed on the surface of the electrocatalyst. In Fig. 3f, the C$_{dl}$ of the v$_s$-Ru-Ni$_9$S$_8$ (65.8 mF cm^{-2}) is much larger than the C$_{dl}$ of the Ru-Ni$_9$S$_8$ (36.8 mF cm^{-2}) and Ni$_9$S$_8$ (16.6 mF cm^{-2}), suggesting the high exposure of accessible active sites on the surface of the v$_s$-Ru-Ni$_9$S$_8$. Electrochemical impedance spectroscopy (EIS) was applied to explore the electrode kinetics in 1.0 M KOH media. The calculated resistances, R$_{ct}$, are as follows: NF (56.5 Ω) > Ni$_9$S$_8$ (16.2 Ω) > Ru-Ni$_9$S$_8$ (8.4 Ω)>v$_s$-Ru-Ni$_9$S$_8$ (2.3 Ω) (Fig. 3e), implying the improved conductivity and charge transfer ability of the v$_s$-Ru-Ni$_9$S$_8$ [57]. In addition, the TOF of the as-prepared catalysts for the OER are 0.21 s^{-1} for the v$_s$-Ru-Ni$_9$S$_8$, 0.13 s^{-1} for the Ru-Ni$_9$S$_8$, and 0.08 s^{-1} for the Ni$_9$S$_8$, respectively, obviously beneficial for the excellent electrocatalytic OER performance of the v$_s$-Ru-Ni$_9$S$_8$ (Fig. S8).

The acidic OER performance of the v$_s$-Ru-Ni$_9$S$_8$ was also tested in 0.5 M H$_2$SO$_4$ electrolyte, but its performance was poor, only an overpotential of 390 mV to reach the current density of 10 mA m^{-2} (Fig. S9).

3.2.2. Universal-pH HER performance

The v$_s$-Ru-Ni$_9$S$_8$ catalyst exhibits the excellent HER catalytic activity over a wide pH range, as shown in Fig. 5a-c. At the current density of 10 mA m^{-2}, the HER overpotentials of the v$_s$-Ru-Ni$_9$S$_8$ are 56 mV in 0.5 M H$_2$SO$_4$ electrolyte, 94 mV in 1 M KOH electrolyte, and 131 mV in 1 M PBS electrolyte (Fig. 5k-m), respectively, surpassing considerably 108, 123, 304 mV of the Ru-Ni$_9$S$_8$, 156, 146, 323 mV of the v$_s$-Ni$_9$S$_8$ and 269, 179, 365 mV of the Ni$_9$S$_8$ and exceeding most of the previously reported HER nickel sulfide electrocatalysts (Table S2 in Supporting

Information), although its catalytic activity is not as good as that of the commercial 20 wt% Pt/C. Apparently, not only the OER performance of the nickel sulfide electrocatalyst but also its HER catalytic activity is remarkably improved due to the synergistic regulation of the trace Ru-doping and sulfur vacancies to electron densities. In Fig. 5d-f, the Tafel slopes of the v$_s$-Ru-Ni$_9$S$_8$ in acidic, alkaline, and neutral media are 71.2, 69.8, and 58.6 mV dec^{-1}, respectively, which are much smaller than those of the Ru-Ni$_9$S$_8$ (81.5, 86.2, and 144.5 mV dec^{-1}), the v$_s$-Ni$_9$S$_8$ (119.1, 88.5, and 143.1 mV dec^{-1}) and the Ni$_9$S$_8$ (130.2, 101.0, and 140.3 mV dec^{-1}). A small Tafel slope confirms that the catalytic reaction kinetics pertains to the Volmer–Heyrovsky mechanism [58]. As illustrated in Fig. 5g-i, the HER durability test for the v$_s$-Ru-Ni$_9$S$_8$ maintains a steady current density (about 14 mA cm^{-2}) in the alkaline electrolyte at the fixed overpotential for 160 h, while that for the commercial Pt/C catalyst is only kept for about 45 h under the same conditions. In acidic and neutral media, the v$_s$-Ru-Ni$_9$S$_8$ catalyst also displays a long-time HER durability and is superior to the commercial Pt/C catalyst. Besides, the LSV curve of the v$_s$-Ru-Ni$_9$S$_8$ after 1000 CV cycles has no apparent attenuation, compared with that before the CV cycles (Fig. S4a), and the high resolution XPS spectrograms (Figs. S5a, S6a and S7a) reveals that the signals of Ni, S, and Ru for the post-HER have been obviously unchanged, also showing the excellent stability of the v$_s$-Ru-Ni$_9$S$_8$ for HER.

3.2.3. Overall water splitting in alkaline electrolyzer

As mentioned earlier, the v$_s$-Ru-Ni$_9$S$_8$ catalyst exhibits the superior bifunctional electrocatalytic activity toward the HER and OER in 1 M KOH media. Therefore, a two-electrode configuration assembled by the v$_s$-Ru-Ni$_9$S$_8$ as bifunctional electrodes, v$_s$-Ru-Ni$_9$S$_8$||v$_s$-Ru-Ni$_9$S$_8$, was served as the evaluation of the overall water splitting activity of the
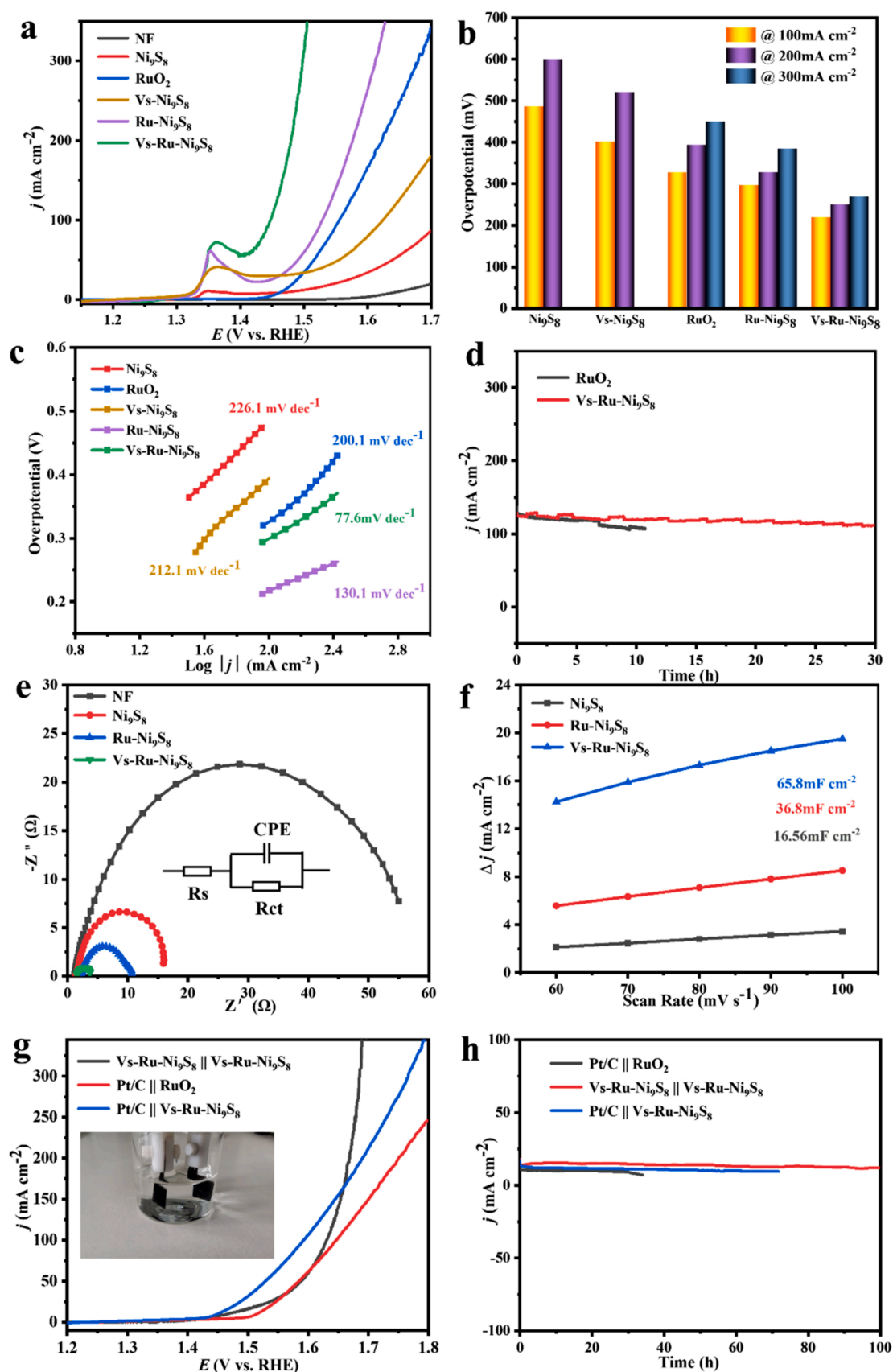
Fig. 3. (a) Polarization curves for OER in 1 M KOH. (b) Overpotentials at 100, 200, and 300 mA·cm^{-2}. (c) Tafel plots. (d) Current density versus time (i-t) curves. (e) ECSA. (f) Nyquist plots. (g) LSV curves of v$_s$-Ru-Ni$_9$S$_8$||v$_s$-Ru-Ni$_9$S$_8$ couple, Pt/C||RuO$_2$ and Pt/C||v$_s$-Ru-Ni$_9$S$_8$ electrodes in 1 M KOH and (h) their current density versus time (i-t) curves.
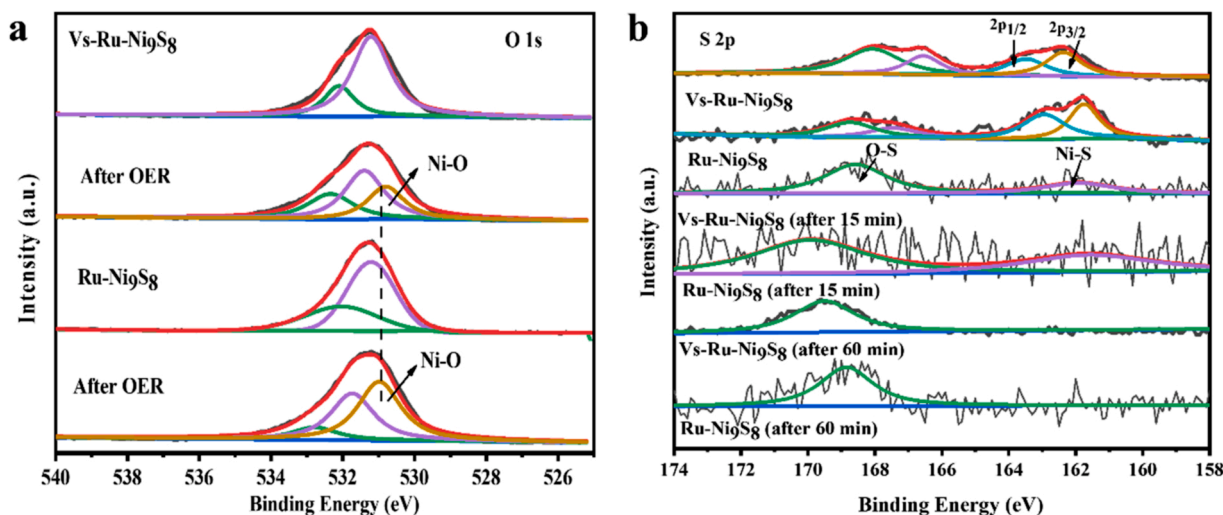
Fig. 4. (a) O 1s XPS spectra of Ru-Ni$_9$S$_8$ and v$_s$-Ru-Ni$_9$S$_8$ before and after OER in 1.0 M KOH media. (b) S 2p XPS spectra of Ru-Ni$_9$S$_8$ and v$_s$-Ru-Ni$_9$S$_8$ after OER stability tests for 15 and 60 min in 1.0 M KOH media.

catalyst. Meanwhile, the Pt/C||v$_s$-Ru-Ni$_9$S$_8$ and Pt/C||RuO$_2$ two-electrode systems were also constructed for comparison. As displayed in Fig. 3g, in 1 M KOH, the assembled v$_s$-Ru-Ni$_9$S$_8$||v$_s$-Ru-Ni$_9$S$_8$ couple requires the cell voltages of 1.47 and 1.63 V to provide the current densities of 10 and 100 mA m^{-2}, respectively, superior to the Pt/C||RuO$_2$ two-electrode couple (1.52 and 1.65 V). Especially, it needs only a voltage of 1.68 V at a higher current density of 300 mA m^{-2}, while the Pt/C||RuO$_2$ couple requires a voltage of 1.88 V. Moreover, when the v$_s$-Ru-Ni$_9$S$_8$ is coupled with the Pt/C, the required cell voltages of the Pt/C||v$_s$-Ru-Ni$_9$S$_8$ for water splitting at 10 and 100 mA cm^{-2} are as low as 1.44 and 1.59 V, significantly surpassing most of the reported state-of-the-art catalysts (Table S3), which demonstrates once again that the v$_s$-Ru-Ni$_9$S$_8$ is a preeminent OER electrocatalyst in alkalinity electrolyte. Moreover, compared with the Pt/C||v$_s$-Ru-Ni$_9$S$_8$ and Pt/C||RuO$_2$ couples, the assembled v$_s$-Ru-Ni$_9$S$_8$||v$_s$-Ru-Ni$_9$S$_8$ couple exhibits a superior stability and a negligible decay is observed for 100 h (Fig. 3h).
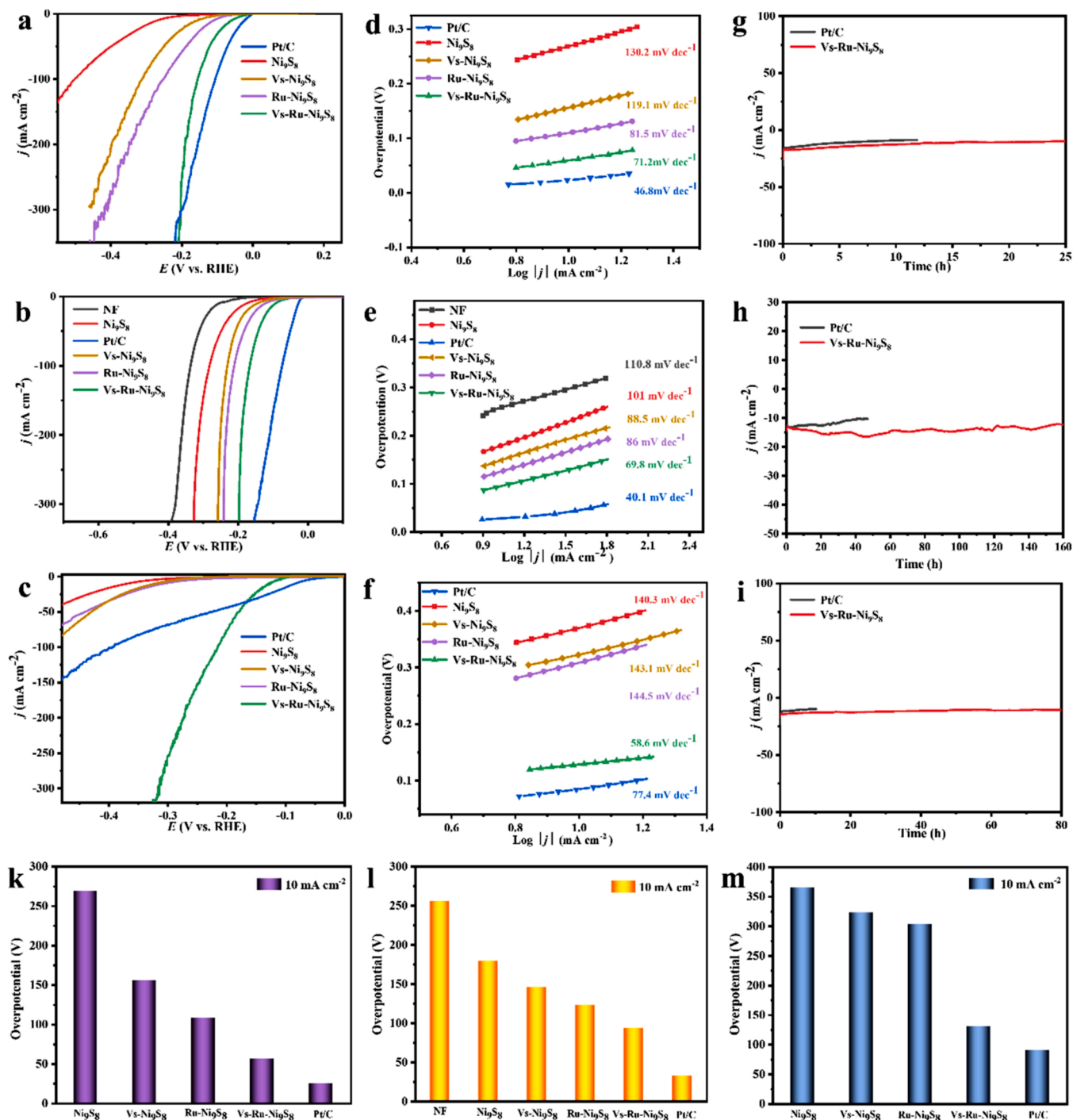
3.3. Theoretical insight into the OER mechanism

The DFT was utilized to analyze the electrocatalytic reaction mechanism for water splitting catalyzed by the v$_s$-Ru-Ni$_9$S$_8$ in detail. The HRTEM image of the catalyst reveals that the (222) crystal plane is the primary exposed crystal plane on the surface of the catalyst (Fig. 1d). The crystal structure for the (222) plane used in computations, its Ru-doped structure, and its doped structure with sulfur vacancies are illustrated in Figs. S13–15. The calculated adsorption Gibbs free energy variations and the projected densities of states (PDOS) for d orbitals of transition metals are shown in Fig. 6. The Gibbs free energy variations for OER were computed by the equations proposed by Nørskov et al. [59], as described in Supporting Information.

As known, the activity of a catalyst depends intensely on the adsorption strength of intermediates on the catalyst and the too-weak or too-strong adsorption results in low catalytic activity [60]. Due to the excessive adsorption of the reaction intermediates for the OER on the pristine Ni$_9$S$_8$, these OER intermediates seem to fall into a very deep potential well, which leads to a considerable low Gibbs free energy variation $\Delta G_{OH}*$ of −1.46 eV for the *OH intermediate and a high free energy change $\Delta G_{OOH}*$ of 3.27 eV for the *OOH intermediate (Fig. 6a). This may be the reason why the pristine Ni$_9$S$_8$ exhibits the poor electrocatalytic performance with a very high calculated OER onset overpotential of 2.04 eV, which is in perfect agreement with the experiment test. By comparison, the Ru-doping weakens significantly the adsorption of the OER intermediates on the Ru-Ni$_9$S$_8$ catalyst by its modulation of

electron density, leading to the moderate surface adsorption strength of the intermediates on the catalyst, which improves remarkably its catalytic performance with a low calculated OER onset overpotential of 0.43 eV. By way of contrast, if the doping Ru atom serves as an active site (the corresponding catalyst is marked as the a$_{Ru}$-Ru-Ni$_9$S$_8$), the surface adsorption of the OER intermediates on the a$_{Ru}$-Ru-Ni$_9$S$_8$ is much stronger than that on the pristine Ni$_9$S$_8$, as shown in Fig. 6a, which results in a lower $\Delta G_{OH}*$ of −2.26 eV for the *OH intermediate and a higher $\Delta G_{OOH}*$ of 4.11 eV for the *OOH intermediate, implying a much worse catalytic activity of the a$_{Ru}$-Ru-Ni$_9$S$_8$ with a calculated onset overpotential of 2.88 eV. It is apparent from these DFT results that the doping Ru atom plays a role in regulating electron density in the OER rather than serves as a catalytic active site.

Introducing sulfur vacancies into the Ru-Ni$_9$S$_8$, on the one hand, can further effectively adjust the surface adsorption strength; on the other hand, it is more important to provide more adsorption sites (active sites) for the OER intermediates, so as to further optimize the catalytic activity. Fig. 6b illustrates the calculated adsorption Gibbs free energy variations ΔG of the v$_s$-Ru-Ni$_9$S$_8$ for the OER, where the a$_{Ni}$-v$_s$-Ru-Ni$_9$S$_8$ and a$_v$-v$_s$-Ru-Ni$_9$S$_8$ represent the catalysts with active sites at a Ni atom and a sulfur vacancy, respectively. As shown, the OER onset overpotential of 0.57 eV of the a$_{Ni}$-v$_s$-Ru-Ni$_9$S$_8$ is higher than 0.43 eV of the Ru-Ni$_9$S$_8$ without sulfur vacancies, seeming that the nickel atom as an active site is not conducive to the improvement of the catalytic activity. Similarly, the onset overpotential of the a$_v$-v$_s$-Ru-Ni$_9$S$_8$ (1.25 eV) is also much higher than that of the Ru-Ni$_9$S$_8$, seeming that a sulfur vacancy cannot also serve as active site. These DFT results seem to indicate that introducing sulfur vacancies into the catalyst would not improve its catalytic activity, which is contrary to the experimental facts. However, carefully investigating two catalytic reaction paths and the Gibbs free energies of the related OER reaction intermediates, it is noted that because the difference between the Gibbs free energies G_O* of the *O intermediate in the two reaction paths is not very big (1.54 eV, Fig. 6c and Table S4), the O atom may migrate from the path for the a$_v$-v$_s$-Ru-Ni$_9$S$_8$ to the path for the a$_{Ni}$-v$_s$-Ru-Ni$_9$S$_8$ through a relatively low energy barrier of 1.54 eV. In other words, in this situation, both Ni atom and sulfur vacancy act as catalytic active sites to synergistically activate the reaction intermediates. In this synergistically catalytic process, a sulfur vacancy first captures and oxidizes OH$^-$ and shears the O-H bond to form O atom, and then O atom migrates from sulfur vacancy to Ni atom through a relatively low energy barrier of 1.54 eV to form *OOH and finally O$_2$, as illustrated in Fig. 6d, which cleverly avoids two high energy barriers of 1.80 and 2.48 eV for the *O and *OOH formations in the

Fig. 6. Adsorption Gibbs free energies of Ni_9S_8, $Ru-Ni_9S_8$, $v_s-Ru-Ni_9S_8$ and their projected densities of states for d orbitals of transition metals, where $a_{Ru}-Ru-Ni_9S_8$, $a_{Ni}-v_s-Ru-Ni_9S_8$, and $a_v-v_s-Ru-Ni_9S_8$ represent the catalysts with active sites at Ru, Ni, and a sulfur vacancy, respectively.

regulation of Ru-doping and sulfur vacancies, the catalyst exhibited an outstanding electrocatalytic performance with an ultra-low OER overpotential of 218 at 100 mA cm^{-2} in alkaline electrolyte and low HER overpotentials over a wide pH range, and a voltage of 1.47 V required to deliver 10 mA cm^{-2} for the $v_s-Ru-Ni_9S_8$ (+,-) cell. Our DFT calculations revealed that the doping Ru atom played a pivotal role in regulating electron density in the OER, rather than served as a catalytic active site. More importantly, we corroborated the active Ni-vacancy pair composed of Ni atom and sulfur vacancy as an active site and its catalytic synergy in the OER. Especially, if a reaction intermediate has similar energies in two reaction paths of the OER, the two reaction paths can cross when this intermediate migrates from one path to another through a low energy barrier, without electron transfer, and the reaction continues towards the low energy barrier direction. Our work provides a simple and efficient strategy for constructing high-performance catalysts.

CRediT authorship contribution statement

Qin Gao: Contributed to the experiment, Data curation, Validation, Writing – original draft. **Wei Luo:** Contributed to the theoretical model designs and computations. **Xueying Ma:** Contributed to the experiment, Data curation, Validation, Writing – original draft. **Zemian Ma:** Contributed to the experiment, Data curation, Validation, Writing – original draft. **Sijun Li:** Contributed to the experiment, Data curation, Validation, Writing – original draft. **Fenglin Gou:** Contributed to the experiment, Data curation, Validation, Writing – original draft. **Wei Shen:** Contributed to the theoretical model designs and computations. **Yimin Jiang:** Contributed to the experiment, Data curation, Validation, Writing – original draft. **Rongxing He:** Contributed to the Conceptualization, Funding acquisition, Supervision, Writing – review & editing. **Ming Li:** Contributed to the Conceptualization, Funding acquisition, Supervision, Writing – review & editing. All authors reviewed and commented on the manuscript before publication.

Declaration of Competing Interest

The authors declare that they have no known competing financial interests or personal relationships that could have appeared to influence the work reported in this paper.

Appendix A. Supplementary material

Supplementary data associated with this article can be found in the online version at doi:10.1016/j.apcatb.2022.121356.

References

[1] Z. Qin, Z. Huang, M. Wang, D. Liu, Y. Chen, L. Guo, Synergistic effect of quantum confinement and site-selective doping in polymeric carbon nitride towards overall water splitting, Appl. Catal. B 261 (2020), 118211.
[2] W. Zhong, S. Shen, M. He, D. Wang, Z. Wang, Z. Lin, W. Tu, J. Yu, The pulsed laser-induced Schottky junction via in-situ forming Cd clusters on CdS surfaces toward efficient visible light-driven photocatalytic hydrogen evolution, Appl. Catal. B 258 (2019), 117967.
[3] A. Xu, W. Tu, S. Shen, Z. Lin, N. Gao, W. Zhong, BiVO4@MoS2 core-shell heterojunction with improved photocatalytic activity for discoloration of Rhodamine B, Appl. Surf. Sci. 528 (2020), 146949.
[4] Y. Jiang, X. Li, S. Yu, L. Jia, X. Zhao, C. Wang, Reduced graphene oxide-modified carbon nanotube/polyimide film supported MoS2 nanoparticles for electrocatalytic hydrogen evolution, Adv. Funct. Mater. 25 (2015) 2693–2700.
[5] Z. Pu, J. Zhao, I.S. Amiinu, W. Li, M. Wang, D. He, S. Mu, A universal synthesis strategy for P-rich noble metal diphosphide-based electrocatalysts for the hydrogen evolution reaction, Energy Environ. Sci. 12 (2019) 952–957.

[6] Y. Liu, K. Zhong, K. Luo, M. Gao, H. Pan, Q. Wang, Size-dependent kinetic enhancement in hydrogen absorption and desorption of the Li−Mg−N−H system, J. Am. Chem. Soc. 131 (2009) 1862–1870.

[7] W. Xia, J. Tang, J. Li, S. Zhang, K.C.W. Wu, J. He, Y. Yamauchi, Defect-rich graphene nanomesh produced by thermal exfoliation of metal–organic frameworks for the oxygen reduction reaction, Angew. Chem. Int. Ed. 58 (2019) 13354–13359.

[8] N.-T. Suen, S.-F. Hung, Q. Quan, N. Zhang, Y.-J. Xu, H.M. Chen, Electrocatalysis for the oxygen evolution reaction: recent development and future perspectives, Chem. Soc. Rev. 46 (2017) 337–365.

[9] Z. Chen, R. Wu, Y. Liu, Y. Ha, Y. Guo, D. Sun, M. Liu, F. Fang, Ultrafine Co nanoparticles encapsulated in carbon-nanotubes-grafted graphene sheets as advanced electrocatalysts for the hydrogen evolution reaction, Adv. Funct. Mater. 30 (2018), 1802011.

[10] Z. Kang, H. Guo, J. Wu, X. Sun, Z. Zhang, Q. Liao, S. Zhang, H. Si, P. Wu, L. Wang, Y. Zhang, Engineering an earth-abundant element-based bifunctional electrocatalyst for highly efficient and durable overall water splitting, Adv. Funct. Mater. 29 (2019), 1807031.

[11] Z. Chen, M. Chen, X. Yan, H. Jia, B. Fei, Y. Ha, H. Qing, H. Yang, M. Liu, R. Wu, Vacancy occupation-driven polymorphic transformation in cobalt ditelluride for boosted oxygen evolution reaction, ACS Nano 14 (2020) 6968–6979.

[12] M. Yu, Z. Wang, J. Liu, F. Sun, P. Yang, J. Qiu, A hierarchically porous and hydrophilic 3D nickel–iron/MXene electrode for accelerating oxygen and hydrogen evolution at high current densities, Nano Energy 63 (2019), 103880.

[13] J. Chang, Q. Lv, G. Li, J. Ge, C. Liu, W. Xing, Core-shell structured Ni12P5/Ni3 (PO4)2 hollow spheres as difunctional and efficient electrocatalysts for overall water electrolysis, Appl. Catal. B 204 (2017) 486–496.

[14] F. Yu, H. Zhou, Y. Huang, J. Sun, F. Qin, J. Bao, W.A. Goddard, S. Chen, Z. Ren, High-performance bifunctional porous non-noble metal phosphide catalyst for overall water splitting, Nat. Commun. 9 (2018) 2551.

[15] X. Jia, Y. Zhao, G. Chen, L. Shang, R. Shi, X. Kang, G.I.N. Waterhouse, L.-Z. Wu, C.-H. Tung, T. Zhang, Ni3FeN nanoparticles derived from ultrathin NiFe-layered double hydroxide nanosheets: an efficient overall water splitting electrocatalyst, Adv. Energy Mater. 6 (2016), 1502585.

[16] F.-C. Shen, S.-N. Sun, Z.-F. Xin, S.-L. Li, L.-Z. Dong, Q. Huang, Y.-R. Wang, J. Liu, Y.-Q. Lan, Hierarchically bimetallic phosphorus doped bimetallic nitrides arrays with unique interfaces for efficient water splitting, Appl. Catal. B 243 (2019) 470–480.

[17] C. Huang, X. Miao, C. Pi, B. Gao, X. Zhang, P. Qin, K. Huo, X. Peng, P.K. Chu, Mo2C/VC heterojunction embedded in graphitic carbon network: An advanced electrocatalyst for hydrogen evolution, Nano Energy 60 (2019) 520–526.

[18] S. Emin, C. Altinkaya, A. Semerci, H. Okuyucu, A. Yildiz, P. Stefanov, Tungsten carbide electrocatalysts prepared from metallic tungsten nanoparticles for efficient hydrogen evolution, Appl. Catal. B 236 (2018) 147–153.

[19] W. Yang, S. Wang, W. Luo, L. Li, J. Hao, W. Shi, Self-supported nickel sulfide derived from nickel foam for hydrogen evolution and oxygen evolution reaction: effect of crystal phase switching, Nanotechnology 32 (2021), 085710.

[20] J. Yu, C. Lv, L. Zhao, L. Zhang, Z. Wang, Q. Liu, Reverse microemulsion-assisted synthesis of NiCo2S4 nanoflakes supported on nickel foam for electrochemical overall water splitting, Adv. Mater. Interfaces 5 (2018), 1701396.

[21] W. Zhu, X. Yue, W. Zhang, S. Yu, Y. Zhang, J. Wang, J. Wang, Nickel sulfide microsphere film on Ni foam as an efficient bifunctional electrocatalyst for overall water splitting, Chem. Commun. 52 (2016) 1486–1489.

[22] T. Kou, S. Wang, J.L. Hauser, S.R.J. Oliver, Y. Ye, J. Guo, Y. Li, Ni foam-supported Fe-doped β-Ni(OH)2 nanosheets show ultralow overpotential for oxygen evolution reaction, ACS Energy Lett. 4 (2019) 622–628.

[23] Z.-F. Huang, J. Song, Y. Du, S. Xi, S. Dou, J.M.V. Nsanzimana, C. Wang, Z.J. Xu, X. Wang, Chemical and structural origin of lattice oxygen oxidation in Co–Zn oxyhydroxide oxygen evolution electrocatalysts, Nat. Energy 4 (2019) 329–338.

[24] X. Xiao, D. Huang, Y. Fu, M. Wen, X. Jiang, X. Lv, M. Li, L. Gao, S. Liu, M. Wang, C. Zhao, Y. Shen, Engineering NiS/Ni2P heterostructures for efficient electrocatalytic water splitting, ACS Appl. Mater. Interfaces 10 (2018) 4689–4696.

[25] B. Fei, Z. Chen, J. Liu, H. Xu, X. Yan, H. Qing, M. Chen, R. Wu, Ultrathinning nickel sulfide with modulated electron density for efficient water splitting, Adv. Energy Mater. 10 (2020), 2001963.

[26] H. Yang, C. Wang, Y. Zhang, Q. Wang, Chemical valence-dependent electrocatalytic activity for oxygen evolution reaction: a case of nickel sulfides hybridized with N and S co-doped carbon nanoparticles, Small 14 (2018).

[27] H. Chen, Z. Yu, R. Jiang, J. Huang, Y. Hou, Y. Zhang, H. Zhu, B. Wang, M. Wang, W. Tang, Sulfur defect rich Mo-Ni3S2 QDs assisted by O-C[double bond, length as m-dash]O chemical bonding for an efficient electrocatalytic overall water splitting, Nanoscale 13 (2021) 6644–6653.

[28] D. Jia, L. Han, Y. Li, W. He, C. Liu, J. Zhang, C. Chen, H. Liu, H.L. Xin, Optimizing electron density of nickel sulfide electrocatalysts through sulfur vacancy engineering for alkaline hydrogen evolution, J. Mater. Chem. A 8 (2020) 18207–18214.

[29] J. Tian, Q. Liu, A.M. Asiri, X. Sun, Self-supported nanoporous cobalt phosphide nanowire arrays: an efficient 3D hydrogen-evolving cathode over the wide range of pH 0–14, J. Am. Chem. Soc. 136 (2014) 7587–7590.

[30] Y. Pan, Y. Liu, Y. Lin, P. Cui, K. Sun, Y. Liu, C. Liu, Cobalt nickel phosphide nanoparticles decorated carbon nanotubes as advanced hybrid catalysts for hydrogen evolution, J. Mater. Chem. A 4 (2016) 14675–14686.

[31] L. Zeng, K. Sun, X. Wang, Y. Liu, Y. Pan, Z. Liu, D. Cao, Y. Song, S. Liu, C. Liu, Three-dimensional-networked Ni2P/Ni3S2 heteronanoflake arrays for highly enhanced electrochemical overall-water-splitting activity, Nano Energy 51 (2018) 26–36.

[32] G. Kresse, J. Furthmüller, Efficient iterative schemes for ab initio total-energy calculations using a plane-wave basis set, Phys. Rev. B 54 (1996) 11169–11186.

[33] J. Zhou, J. Zhao, R. Liu, Defect engineering of zeolite imidazole framework derived ZnS nanosheets towards enhanced visible light driven photocatalytic hydrogen production, Appl. Catal. B 278 (2020), 119265.

[34] Q. Wu, Q. Zheng, R. van de Krol, Creating oxygen vacancies as a novel strategy to form tetrahedrally coordinated Ti4+ in Fe/TiO2 nanoparticles, J. Phys. Chem. C 116 (2012) 7219–7226.

[35] D. Chen, Z. Pu, R. Lu, P. Ji, P. Wang, J. Zhu, C. Lin, H.-W. Li, X. Zhou, Z. Hu, F. Xia, J. Wu, S. Mu, Ultralow Ru loading transition metal phosphides as high-efficient bifunctional electrocatalyst for a solar-to-hydrogen generation system, Adv. Energy Mater. 10 (2020), 2000814.

[36] Y. Xu, X. Jiang, G. Shao, H. Xiang, S. Si, X. Li, T.S. Hu, G. Hong, S. Dong, H. Li, Y. Feng, S. Liu, Interface effect of Ru-MoS2 nanoflowers on lignin substrate for enhanced hydrogen evolution activity, Energy Environ. Mater. 4 (2021) 117–125.

[37] C. Zhang, Y. Shi, Y. Yu, Y. Du, B. Zhang, Engineering sulfur defects, atomic thickness, and porous structures into cobalt sulfide nanosheets for efficient electrocatalytic alkaline hydrogen evolution, ACS Catal. 8 (2018) 8077–8083.

[38] Y. Yin, J. Han, Y. Zhang, X. Zhang, P. Xu, Q. Yuan, L. Samad, X. Wang, Y. Wang, Z. Zhang, P. Zhang, X. Cao, B. Song, S. Jin, Contributions of phase, sulfur vacancies, and edges to the hydrogen evolution reaction catalytic activity of porous molybdenum disulfide nanosheets, J. Am. Chem. Soc. 138 (2016) 7965–7972.

[39] Y. He, P. Zhang, H. Huang, X. Li, X. Zhai, B. Chen, Z. Guo, Engineering sulfur vacancies of Ni3S2 nanosheets as a binder-free cathode for an aqueous rechargeable Ni-Zn battery, ACS Appl. Energy Mater. 3 (2020) 3863–3875.

[40] A. Sivanantham, P. Ganesan, S. Shanmugam, Hierarchical NiCo2S4 nanowire arrays supported on Ni foam: an efficient and durable bifunctional electrocatalyst for oxygen and hydrogen evolution reactions, Adv. Funct. Mater. 26 (2016) 4661–4672.

[41] L. Mi, W. Wei, S. Huang, S. Cui, W. Zhang, H. Hou, W. Chen, A nest-like Ni@ Ni1.4Co1.6S2 electrode for flexible high-performance rolling supercapacitor device design, J. Mater. Chem. A 3 (2015) 20973–20982.

[42] H. Xu, C. Shan, X. Wu, M. Sun, B. Huang, Y. Tang, C.-H. Yan, Fabrication of layered double hydroxide microcapsules mediated by cerium doping in metal–organic frameworks for boosting water splitting, Energy Environ. Sci. 13 (2020) 2949–2956.

[43] G. Chen, T. Wang, J. Zhang, P. Liu, H. Sun, X. Zhuang, M. Chen, X. Feng, Accelerated hydrogen evolution kinetics on NiFe-layered double hydroxide electrocatalysts by tailoring water dissociation active sites, Adv. Funct. Mater. 30 (2018), 1706279.

[44] N. Xie, D.-D. Ma, X.-T. Wu, Q.-L. Zhu, Facile construction of self-supported Fe-doped Ni3S2 nanoparticle arrays for the ultralow-overpotential oxygen evolution reaction, Nanoscale 13 (2021) 1807–1812.

[45] L. Shen, L. Wang, G. Xu, H. Li, H. Dou, X. Zhang, NiCo2S4 nanosheets grown on nitrogen-doped carbon foams as an advanced electrode for supercapacitors, Adv. Energy Mater. 5 (2015).

[46] W.-Z. Chen, P.-Y. Liu, L. Zhang, Y. Liu, Z. Liu, J. He, Y.-Q. Wang, High-efficient and durable overall water splitting performance by interfacial engineering of Fe-doped urchin-like Ni2P/Ni3S2 heterostructure, Chem. Eng. J. 424 (2021) 130434.

[47] Y. Liu, Z. Li, L. Yao, S. Chen, P. Zhang, L. Deng, Confined growth of NiCo2S4 nanosheets on carbon flakes derived from eggplant with enhanced performance for asymmetric supercapacitors, Chem. Eng. J. 366 (2019) 550–559.

[48] J. Su, Y. Yang, G. Xia, J. Chen, P. Jiang, Q. Chen, Ruthenium-cobalt nanoalloys encapsulated in nitrogen-doped graphene as active electrocatalysts for producing hydrogen in alkaline media, Nat. Commun. 8 (2017) 14969.

[49] W. Zhou, X.-J. Wu, X. Cao, X. Huang, C. Tan, J. Tian, H. Liu, J. Wang, H. Zhang, Ni3S2 nanorods/Ni foam composite electrode with low overpotential for electrocatalytic oxygen evolution, Energy Environ. Sci. 6 (2013) 2921–2924.

[50] C. Tang, N. Cheng, Z. Pu, W. Xing, S. Sun, NiSe nanowire film supported on nickel foam: an efficient and stable 3D bifunctional electrode for full water splitting, Angew. Chem. Int. Ed. 54 (2015) 9351–9355.

[51] C. Liang, P. Zou, A. Nairan, Y. Zhang, J. Liu, K. Liu, S. Hu, F. Kang, H.J. Fan, C. Yang, Exceptional performance of hierarchical Ni–Fe oxyhydroxide@NiFe alloy nanowire array electrocatalysts for large current density water splitting, Energy Environ. Sci. 13 (2020) 86–95.

[52] X. Cheng, C. Lei, J. Yang, B. Yang, Z. Li, J. Lu, X. Zhang, L. Lei, Y. Hou, K. Ostrikov, Efficient electrocatalytic oxygen evolution at extremely high current density over 3D ultrasmall zero-valent iron-coupled nickel sulfide nanosheets, ChemElectroChem 5 (2018) 3866–3872.

[53] Q. Qin, L. Chen, T. Wei, X. Liu, MoS2/NiS yolk–shell microsphere-based electrodes for overall water splitting and asymmetric supercapacitor, Small 15 (2019), 1803639.

[54] Z. Dai, Z. Geng, H. Jiang, J. Wang, Y. Luo, B. Li, Y. Zong, J. Yang, Y. Guo, Y. Zheng, X. Wang, Q. Yan, Hexagonal-phase cobalt monophosphosulfide for highly efficient overall water splitting, ACS Nano 11 (2017) 11031–11040.

[55] J. Zhang, T. Wang, D. Pohl, B. Rellinghaus, R. Dong, S. Liu, X. Zhuang, X. Feng, Interface engineering of MoS2/Ni3S2 heterostructures for highly enhanced electrochemical overall-water-splitting activity, Angew. Chem. Int. Ed. 55 (2016) 6702–6707.

[56] K. Wu, K. Sun, S. Liu, W.-C. Cheong, Z. Chen, C. Zhang, Y. Pan, Y. Cheng, Z. Zhuang, X. Wei, Y. Wang, L. Zheng, Q. Zhang, D. Wang, Q. Peng, C. Chen, Y. Li, Atomically dispersed Ni–Ru–P interface sites for high-efficiency pH-universal electrocatalysis of hydrogen evolution, Nano Energy 80 (2021), 105467.

[57] W. Hao, R. Wu, R. Zhang, Y. Ha, Z. Chen, L. Wang, Y. Yang, X. Ma, D. Sun, F. Fang, Y. Guo, Electroless plating of highly efficient bifunctional boride-based electrodes toward practical overall water splitting, Adv. Energy Mater. 8 (2018), 1801372.

[58] H. Zhang, X. Li, A. Hähnel, V. Naumann, C. Lin, S. Azimi, S.L. Schweizer, A. W. Maijenburg, R.B. Wehrspohn, Bifunctional heterostructure assembly of NiFe

LDH nanosheets on NiCoP nanowires for highly efficient and stable overall water splitting, Adv. Funct. Mater. 28 (2018), 1706847.

[59] I.C. Man, H.Y. Su, F. Calle-Vallejo, H.A. Hansen, J.I. Martínez, N.G. Inoglu, J. Kitchin, T.F. Jaramillo, J.K. Nørskov, J. Rossmeisl, Universality in oxygen evolution electrocatalysis on oxide surfaces, ChemCatChem 3 (2011) 1159–1165.

[60] A.J. Medford, A. Vojvodic, J.S. Hummelshøj, J. Voss, F. Abild-Pedersen, F. Studt, T. Bligaard, A. Nilsson, J.K. Nørskov, From the Sabatier principle to a predictive theory of transition-metal heterogeneous catalysis, J. Catal. 328 (2015) 36–42.

[61] A. Ruban, B. Hammer, P. Stoltze, H.L. Skriver, J.K. Nørskov, Surface electronic structure and reactivity of transition and noble metals1Communication presented at the First Francqui Colloquium, Brussels, 19–20 February 1996.1, J. Mol. Catal. A Chem. 115 (1997) 421–429.

[62] X. Mao, C. Ling, C. Tang, C. Yan, Z. Zhu, A. Du, Predicting a new class of metal-organic frameworks as efficient catalyst for bi-functional oxygen evolution/reduction reactions, J. Catal. 367 (2018) 206–211.